Original Paper

Eletrônica de Potência
Open Journal of Power Electronics



Received September 04, 2026; Received in revised form October 28, 2026; Accepted November 11, 2026; Date of publication November 18, 2026.
The review of this paper was arranged by Associate Editor Jéssika M. de Andrade and Editor-in-Chief Allan F. Cupertino.
Digital Object Identifier http://doi.org/10.18618/REP.e202643

Data Acquisition System for the Experimental Assessment of a Hybrid Photovoltaic Thermal Plant: Characterization, Model Validation, and Control Simulation with Real Data

Carlos R. Coutinho[1,*], Rodrigo Fiorotti[1], Gustavo B. Coutinho[1], Jussara F. Fardin[2], Helder R. de O. Rocha[2]

[1]Federal Institute of Espírito Santo, Campus São Mateus, São Mateus – ES, Brasil.
[2]Federal University of Espírito Santo, Campus Goiabeiras, Vitória – ES, Brasil.

e-mail: crcoutinho@ifes.edu.br*; rodrigo.fiorotti@ifes.edu.br; gbonacoutinho@icloud.com; jussara.fardin@ufes.br; helder.rocha@ufes.br.
*Corresponding author.

ABSTRACT Photovoltaic (PV) and hybrid photovoltaic/thermal (PVT) systems are competitive clean-generation technologies, but their experimental assessment requires the reliable, simultaneous measurement of electrical, thermal, and environmental quantities. The main contribution of this work is a microcontroller-based data acquisition system, with redundant local storage and cloud transmission, installed in an experimental plant with two PV and two PVT modules. Extending previous results, the system is evaluated over 22 days of continuous operation (30,297 samples), achieving 99.1% completeness and only 0.02% of spurious samples. To demonstrate its capabilities, the collected data are used to validate a temperature-corrected electrical model, with a daily-energy error between 4.7% and 7.6%, to thermally characterize the PVT collector from a forced-circulation test, and to propagate measurement uncertainties to the efficiencies. The collector model, fed with real measured series, then simulates forced circulation over the 18 thermosiphon days, estimating a potential gain of 96% (79% net), an upper bound that depends on hot-water consumption. A control simulation shows that the operating strategy is decisive: kept continuously on, the pump saturates the reservoir and wastes pumping, whereas judicious actuation preserves the gain. The validated model and the open dataset support embedded, model-based monitoring and control of the plant.

KEYWORDS Data acquisition, energy conversion, energy efficiency, hybrid photovoltaic/thermal systems, instrumentation, photovoltaic systems.

I. INTRODUCTION

In the pursuit of promoting access to clean and affordable energy, the deployment of distributed generation (DG) systems based on photovoltaic (PV) technology has shown significant growth in recent years. In Brazil, in 2023, PV generation accounted for 7% of the electricity mix, growing 68.1% relative to 2022 [1].

Although solar irradiation is an abundant and widely available resource, only a small fraction of the incident energy is converted into electricity by photovoltaic cells, whose commercial module efficiency typically remains below 23% [2]. Most of the incident energy is converted into heat and dissipated by the cell, degrading the performance of the PV system [3].

Given this available thermal energy, hybrid photovoltaic/thermal (PV/T) systems emerge, characterized by the integration of photovoltaic technology with a solar thermal collector, aiming to maximize the energy harvesting from solar irradiation. Among the different constructive forms, a flat PV/T module consists of a PV module with a heat exchanger attached to its backsheet [4]. A working fluid, e.g. water, circulates through the exchanger, which, besides cooling the module, can be used in low-temperature applications [5]. PV/T systems can harness a large part of the incident solar energy spectrum, potentially reaching an overall efficiency between 70% and 80% [6], [7]. It should be noted that this overall efficiency is not a photovoltaic conversion efficiency: it is defined as the sum of the electrical and thermal efficiencies, as in (6). The electrical share remains bounded by the photovoltaic conversion limit, and the high overall value stems mostly from the recovered heat, which is also accounted for as useful energy.

The experimental assessment of PV and PV/T technologies relies on data acquisition (DAQ) systems that measure electrical, thermal, and environmental quantities simultaneously and reliably over long campaigns. Low-cost

CC BY

microcontroller-based dataloggers, e.g. based on Arduino, have become common for monitoring photovoltaic systems [8], [9], and some works add remote data transmission based on the Internet of Things (IoT) [10]. These solutions, however, are typically reported mainly at the hardware level: few of them quantify the quality of the acquisition itself in long-term operation (completeness, data loss, and spurious-sample rate) or demonstrate the use of the collected data for model validation and for the synthesis of control strategies. This work addresses that gap by presenting a DAQ system and, from its own data, assessing its reliability and demonstrating a chain of quantitative analyses enabled by it.

This paper is an extended version of a previous work by the authors [11], in which the acquisition hardware and two illustrative days of operation were reported. The main objective of this paper is the data acquisition system itself: its architecture, its metrological characterization, and its reliability in continuous operation. The other analyses use only the data produced by the system and are presented as demonstrations of what it makes possible. Accordingly, the contributions are:

- *The acquisition system and its reliability:* a low-cost DAQ with redundant local and cloud storage, whose acquisition quality is quantified over 22 days of continuous operation (30,297 samples) in terms of completeness, sampling gaps, and spurious-sample rate, a step rarely reported for such systems.
- *Its metrological characterization:* the propagation of the sensor and analog-to-digital (A/D) converter uncertainties up to the electrical and thermal efficiencies, identifying the quantities that limit the accuracy of each figure of merit.
- *Demonstrations of use*, based solely on the acquired data: (i) the validation of a temperature-corrected electrical model for the four modules; (ii) the in-situ identification of the PV/T collector parameters through the Hottel–Whillier curve, from a forced-circulation test; and (iii) forced-circulation and pump-control simulations driven by the measured series, illustrating how the data support design and operation decisions.

The numerical results of these demonstrations, such as the collector parameters and the estimated forced-circulation gain, are reported with their limitations and should be read as illustrations of the system's capabilities rather than as general characterizations of the technology. As the system is a permanent installation in continuous operation, any of these analyses can be repeated and refined with new campaigns, without additional instrumentation effort.

Compared with [11], which reported only the acquisition hardware and two illustrative operating days processed offline, the present version keeps the description of the plant and hardware for self-containedness and adds: the reliability characterization over the 22-day campaign; the propagation of the sensor and A/D uncertainties up to the efficiencies; the validation of a temperature-corrected electrical model for the four modules; the experimental Hottel–Whillier characterization of the PV/T collector; the forced-circulation simulation over the thermosiphon days; and the pump-actuation control simulation. All analyses are fully reproducible from the open dataset [12].

II. PV AND PV/T SYSTEMS

A. PV Systems

The conversion of solar irradiation into electricity in photovoltaic systems occurs through the photovoltaic effect, when cells made of semiconductor materials absorb the energy of photons and release electrons [13]. According to [14], the electrical efficiency is computed by (1) using the measured values of voltage (V), current (I), and irradiance (G):

$$\eta_{el}(i) = \frac{P_{el}(i)}{G(i) \cdot S} = \frac{V(i) \cdot I(i)}{G(i) \cdot S} \tag{1}$$

where i is the sample index, $V(i)$, $I(i)$ and $G(i)$ are, respectively, the voltage, current and incident irradiance in the plane of the modules measured at sample i, P_{el} is the electrical power and S the effective area of the PV module (1.984 m^2).

The expected power at the maximum power point (MPP) of a module can be estimated by the temperature-correction model [15], [16]:

$$P_{mp} = k \cdot P_{STC} \, \frac{G}{G_{STC}} \left[1 + \gamma \left(T_c - 25\right)\right] \tag{2}$$

where P_{STC} is the nominal power under standard test conditions (G_{STC} = 1000 W/m^2, 25 °C), γ the power temperature coefficient, T_c the cell temperature, and k an effective performance factor that lumps together systematic losses (soiling, cabling, mismatch, aging, and MPP deviation). In the absence of a direct measurement of T_c, it is estimated from the ambient temperature T_{amb} and the nominal module operating temperature (NMOT):

$$T_c = T_{amb} + \frac{(\mathrm{NMOT} - 20)}{800} \, G. \tag{3}$$

B. PV/T Systems

As in the PV system, the electrical efficiency of the PV/T is computed by (1). However, part of the heat dissipated in the module is transferred to a working fluid that flows through the heat exchanger, by natural (thermosiphon effect) or forced circulation [17]. The absorbed thermal energy can be stored as hot water in reservoirs for later use.

The thermal efficiency η_{th} is defined as the ratio between the thermal energy transferred to the fluid Q_u and the incident energy [17]:

$$\eta_{th} = \frac{Q_u}{G \cdot S_{th}} \tag{4}$$

where S_{th} is the area of the heat exchangers attached to the PV/T modules (1.8 m^2 per module; 3.6 m^2 for the two PV/T modules, which share the measured flow), with the useful heat Q_u related to the mass flow rate $\dot{m}$, the specific

heat C_p, and the outlet T_o and inlet T_i temperatures of the exchanger [18]:

$$Q_u = \dot{m} \cdot C_p \cdot (T_o - T_i). \tag{5}$$

A common simplification for the overall efficiency is [19]:

$$\eta_{total} = \eta_{el} + \eta_{th}. \tag{6}$$

Under quasi-steady-state conditions, the thermal performance of a collector can be described by the Hottel–Whillier equation [17]:

$$\eta_{th} = F_R(\tau\alpha) - F_R U_L \frac{(T_i - T_{amb})}{G} \tag{7}$$

where F_R is the collector heat-removal factor, $(\tau\alpha)$ is the effective transmittance–absorptance product of the cover–absorber set (not a functional argument), so that the product $F_R(\tau\alpha)$ represents the effective optical efficiency, and $F_R U_L$ is the overall thermal loss coefficient of the collector, with U_L the overall heat-loss coefficient. The experimental identification of these parameters allows comparing the collector with the literature and feeding system simulations.

III. MATERIALS AND METHODS

This section describes the experimental photovoltaic/thermal plant and the data acquisition system developed to monitor it, including the instrumentation, the hardware and firmware architecture, and the uncertainty treatment. Next, the analysis methodology applied to the collected data, which underlies the results presented afterward, is detailed.

A. Data Acquisition System

The system was developed in an experimental plant installed at the Federal Institute of Espírito Santo (IFES), São Mateus campus[1], Figure 1, which comprises four photovoltaic modules, model CS3W-425, manufactured by Canadian Solar. In two of the modules, RollBond-type heat exchangers were attached to the backsheet, turning them into PV/T modules that generate thermal energy in addition to electricity. The modules are connected to an APSsystem QS1A microinverter, with a maximum power of 1500 W and four independent channels, extracting the maximum electrical power from each module independently. The thermal energy captured by the heat exchangers is stored as heated water in a 200-liter boiler, emulating a real residential application.

To monitor each system variable and assess the performance of the technologies, a data acquisition system was assembled using the Arduino Mega 2560 microcontroller, to which the sensors of each variable are connected. The collected data are saved to a local micro Secure Digital (SD) card and also transmitted to a cloud database through an ESP32 connected to the communication port. Figure 2 outlines the interconnection of the sensors to the microcontroller and to the PV and PV/T systems.

[1]Approximate location: 18.68°S, 39.86°W (São Mateus, Espírito Santo, Brazil). The measurement campaign reported here was carried out between September and October 2024.



FIGURE 1. Experimental photovoltaic/thermal plant installed at IFES, São Mateus campus.

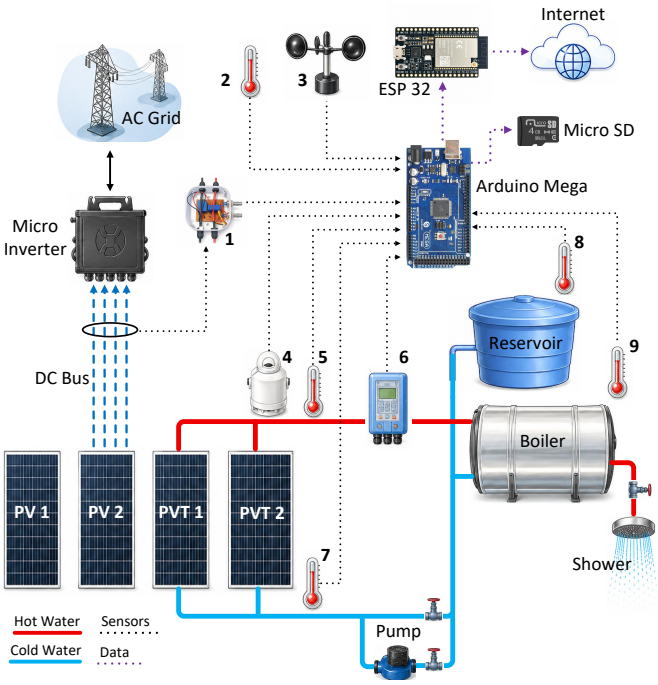

FIGURE 2. Diagram of the acquisition system: interconnection of the sensors to the microcontroller and to the PV and PV/T systems, with the data flow to the cloud database. (1) voltage (V) and current (I) sensors; (2) ambient temperature (T_{amb}); (3) wind speed; (4) solar irradiance (G); (5) heat-exchanger outlet temperature (T_o); (6) mass flow rate ($\dot{m}$); (7) heat-exchanger inlet temperature (T_i); (8) reservoir temperature (T_{res}); (9) boiler temperature (T_{boiler}).

The voltage of each module is measured with the LV 20-P (LEM) sensor, based on the Hall effect, with an accuracy of $\pm 1\%$ and a linearity error below 0.2%. The generated current is monitored with the LA 55-P (LEM) sensor, with an accuracy of $\pm 0.65\%$ and a linearity error below 0.15%. The analog signals from these sensors are digitized by the 10-bit A/D converter of the Arduino Mega ($V_{ref} = 5$ V), with the conditioning ranges adjusted to use most of the converter's full scale (voltage and current up to 4.5 V).

CC BY

The temperatures are measured by digital DS18B20 sensors with a 12-bit resolution (0.0625 °C) and an absolute accuracy of ±0.5 °C, at five distinct points: heat-exchanger inlet (T_i), exchanger outlet (T_o), reservoir (T_{res}), boiler (T_{boiler}), and ambient temperature (T_{amb}). The solar irradiance G is measured by the class-B pyranometer SR05-D1A3 (Hukseflux), which measures from 0 to 1.6 kW/m^2, with a calibration uncertainty below 2.4% for $k = 2$. The mass flow rate $\dot{m}$ is monitored by the ECR MTDS-100F ultrasonic sensor, configured from 0 to 0.2 L/s, with an accuracy of 0.1%. The wind speed is measured by the AN-4A anemometer, configured from 0 to 42 m/s, with an accuracy of ±3%.

The Arduino microcontroller cyclically performs the sequential reading of twenty samples for each quantity through analog channels (voltage, current, irradiance, flow rate, and wind speed) and digital channels (DS18B20 temperature sensors via the 1-Wire bus). The signals are then processed by computing the moving average of the samples and converted to their respective physical units, and the electrical power of each module is also computed.

The measured values, together with their respective timestamp (date and time of collection), are grouped into a single record structured in JavaScript Object Notation (JSON) format. These data are stored locally on a micro SD card, serving as a backup copy, and transmitted via serial interface to the ESP32 module, which publishes them to the Firebase database. Every day, data acquisition is paused between 23:17 and 23:22 to allow the system to consolidate and save the day's records to a separate file in the cloud.

For this study, the daily files were consolidated into a single spreadsheet and organized in tabular form, with each variable allocated to its respective column. The local (SD)/cloud redundancy ensures that connectivity failures do not cause data loss, only synchronization delay.

B. Uncertainty Propagation

Since the efficiencies are quantities derived from multiple measurements, their combined relative uncertainty is obtained by the uncertainty propagation law of the *Guide to the Expression of Uncertainty in Measurement* (GUM) [20], which, for a quantity $y = f(x_1, \ldots, x_n)$ with uncorrelated input variables, yields $u_c^2(y) = \sum_i (\partial f/\partial x_i)^2\, u^2(x_i)$. Applying it to (1) and (4)–(5), the combined relative uncertainties are obtained:

$$\frac{u(\eta_{el})}{\eta_{el}} = \sqrt{\left(\tfrac{u_V}{V}\right)^2 + \left(\tfrac{u_I}{I}\right)^2 + \left(\tfrac{u_G}{G}\right)^2} \tag{8}$$

$$\frac{u(\eta_{th})}{\eta_{th}} = \sqrt{\left(\tfrac{u_{\dot{m}}}{\dot{m}}\right)^2 + \frac{u_{T_o}^2 + u_{T_i}^2}{(T_o - T_i)^2} + \left(\tfrac{u_G}{G}\right)^2}. \tag{9}$$

Here, u_X denotes the standard uncertainty of quantity X. It is noted in (9) that the temperature-difference uncertainty dominates when $T_o - T_i$ is small, a typical situation at times when the two temperatures are very close, generally at the beginning and end of the day.

C. Analysis Methodology

The acquisition system was evaluated over a continuous period of 22 days, of which 20 were complete, under natural and varied environmental conditions: the daily irradiation in the plane of the modules ranged from overcast to clear-sky days (peak irradiance up to 1430 W/m^2), the ambient temperature varied between 18 °C and 35 °C, and the other meteorological quantities followed the typical dynamics of the site. This diversity of conditions makes it possible to evaluate the system and the models under scenarios representative of real operation, and not only under idealized situations. The raw data (1 min) are aggregated into 5 min averages. The 5 min window was chosen as a compromise: it is long enough to attenuate the predominantly random sensor noise (which, for N averaged samples, decreases as $1/\sqrt{N}$) and the sub-minute fluctuations, being of the same order as the averaging periods used in collector testing according to ISO 9806 [21], yet short enough to preserve the diurnal dynamics and the cloud transients that are relevant to the electrical-model validation. As a sensitivity check, windows of 1 and 10 min were also evaluated: the performance factors k of the electrical model changed by less than 0.2%, $F_R(\tau\alpha)$ by up to 6% and $F_R U_L$ by up to 10%, and the estimated gross forced-circulation gain ranged from $+85\%$ to $+98\%$, so that the conclusions are unchanged. The following steps describe the analyses performed on the data collected by the system, corresponding to the demonstrations of the capability of the data acquisition system.

- *Uncertainty propagation.* The sensor uncertainties, including the 10-bit A/D converter quantization, are propagated by (8)–(9) up to the efficiencies. As it permeates all measured quantities, this analysis contextualizes the reliability of the remaining results (Subsection B).
- *Cleaning and synchronization.* Each record gathers the 20 measured quantities with a timestamp. Samples with temperature-reading failures (values outside the valid physical range, typical of a transient interruption of the 1-Wire bus) are discarded by range checking. The completeness and the removed-sample rate are quantified in Subsection C.
- *Electrical model validation.* The power of each module is modeled by (2)–(3); the effective performance factor k is fitted by least squares over 5 min averages with significant irradiance ($G > 50$ W/m^2). The quality is measured by the root-mean-square error (RMSE), the mean absolute percentage error (MAPE), and the coefficient of determination (R^2) of the instantaneous power and by the error of the integrated daily energy (Subsection D).
- *Collector thermal characterization.* The Hottel–Whillier curve (7) presumes a forced, constant, and known flow rate. Over the period, the system operated mostly in thermosiphon mode (natural circulation, flow rate of ≈7 g/s, self-induced by the temperature difference). A single day corresponds to a forced-

circulation test with a pump (flow rate of ≈110 g/s between 09:00 and 15:00), a condition in which the equation's premise is satisfied. For this reason, the collector model is fitted exclusively with the forced-circulation day, using the 5-min windows in which the pump was running throughout, discarding the first 15 min after the pump start-up, with $G > 400$ W/m^2 and $T_o > T_i$ (Subsection E).

- *Forced-circulation simulation.* The collector model is fed with the real series of G, T_{amb}, and T_i from the 18 thermosiphon days, estimating the thermal energy that forced circulation would have captured. On two Sundays of the campaign, the pump was switched on by its timer from 07:00 to 24:00 (flow rate of ≈43 g/s); these days are therefore not thermosiphon days and are used instead as an independent check of the collector model. The timer also switched the pump on daily for about 25 min from 07:00, at low irradiance, a period that accounts for only 1.7% of the thermal energy measured on the thermosiphon days. This estimate is compared with the thermal energy *actually measured* in thermosiphon mode on the same days, quantifying the gain (Subsection F).
- *Control simulation.* Over the forced-circulation day, two pump-actuation strategies are compared (continuously on, as in the test, and controlled by a threshold on the temperature difference $T_o - T_i$), evaluating the net thermal energy and the pumping hours (Subsection G).

IV. RESULTS AND DISCUSSION

A. System Operation

The instantaneous values of each quantity are recorded with a sampling period of approximately 1 minute, providing high-resolution information on the performance of the PV and PV/T systems. The data can be accessed as a file in the cloud database, with daily backup, or in real time as shown in Figure 3.



FIGURE 3. Real-time data monitoring screen (Firebase console): each record contains the timestamp followed by the 20 measured quantities.

Figure 4 shows the typical behavior of the PV and PV/T systems over a day, from the data recorded by the acquisition system. As solar irradiance rises during the morning, the generated electrical power and the temperatures of the PV/T system increase. Whereas the PV module converts solar radiation exclusively into electricity, the PV/T system simultaneously performs the photovoltaic conversion and the heat recovery, transferring it to the water through the heat exchanger. This process results in the gradual increase of the reservoir temperature over the operating period, Figure 4(a). The useful thermal power, Figure 4(b), follows the availability of radiation and the fluid circulation, while the PV/T outlet temperature remains above the inlet temperature during much of the solar period. The data thus demonstrate the integrated operation of the electrical and thermal conversions characteristic of the PV/T system.

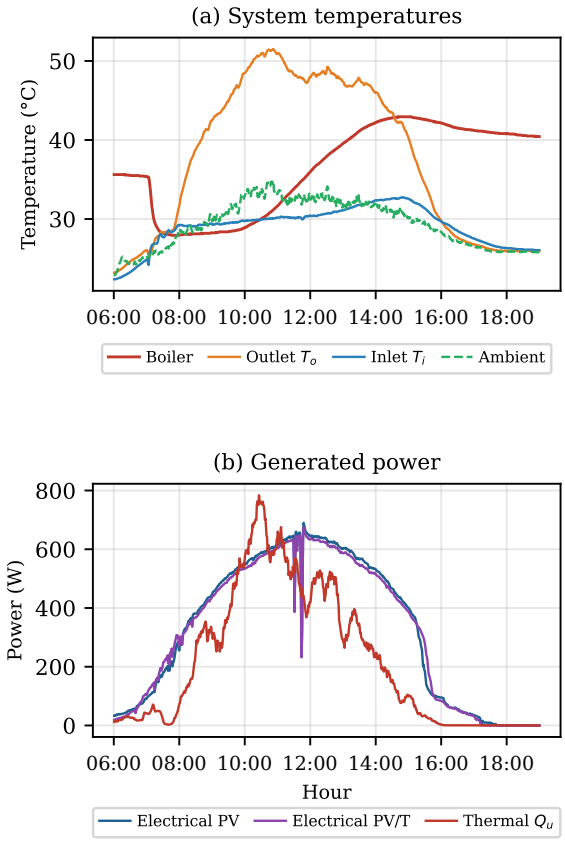

FIGURE 4. Operational behavior of the PV and PV/T systems obtained from the acquisition-system data: (a) system temperatures and (b) electrical and thermal power over the day.

B. Efficiency Uncertainty Analysis

The measurement uncertainty was evaluated according to the GUM recommendations [20]. Table 1 presents, for each quantity, the standard uncertainty associated with calibration (u_{cal}), the A/D converter quantization uncertainty (u_q), the combined standard uncertainty (u_c), obtained by the quadratic combination of these components, and the expanded uncertainty (U), computed for a coverage factor $k = 2$ and expressed relative to the full scale. It is found that the contribution of the 10-bit quantization is negligible compared with calibration in all channels, since the conditioning ranges use most of the converter's full scale. For the differential measurement $T_o - T_i$, it is assumed

CC BY

that the systematic absolute-accuracy error of the DS18B20 sensors (± 0.5 °C), being of the same model, cancels out in the difference, leaving the 12-bit resolution as the effective uncertainty. This assumption is supported by the nature of the DS18B20: the ± 0.5 °C figure is a worst-case bound over the full -10 to $+85$ °C range, and for two sensors of the same part operating at close temperatures (the inlet and outlet of the same exchanger, typically 1 to 12 °C apart) the systematic components are strongly correlated and largely common-mode, so they are substantially removed in the subtraction. It should nevertheless be noted that, without a paired calibration, the residual, non-common part of this error is not quantified. Its effect on the results was therefore assessed by imposing a residual offset of ± 0.1 °C between the inlet and outlet readings. In thermosiphon mode, where $T_o - T_i$ is typically about 12 °C, the measured thermal energy changes by only $\pm 2\%$. In the forced-circulation test, where $T_o - T_i$ is about 1 °C, $F_R(\tau\alpha)$ changes by about $\pm 5\%$, $F_R U_L$ is practically unaffected, and the estimated forced-circulation gain (Subsection F) changes by at most about ± 10 percentage points, so that the qualitative conclusions are preserved. A paired (two-point) calibration of the inlet/outlet sensors is recommended to bound this residual error and is proposed as future work.

TABLE 1. Sensor uncertainty referred to the full scale (FS).

Quantity	Range	u_{cal}	u_q	u_c	U/FS (%)
Voltage (V)	0–56	0.28	0.018	0.2805	1.00
Current (A)	0–50	0.1625	0.016	0.1633	0.65
Irradiance (W/m^2)	0–1600	19.2	2.3	19.33	2.42
Temperature (°C)	-10–85	0.01804	0	0.01804	0.04
Flow rate (L/s)	0–0.2	0.0001	0	0.0001	0.10
Wind (m/s)	0–42	0.63	0.0059	0.63	3.00

Propagating the uncertainties of Table 1 through Eqs. (8)–(9), but referred to the values measured under typical operating conditions rather than to the full scale, more representative estimates of the uncertainty actually associated with the computed efficiencies are obtained. For the electrical efficiency, considering a point near the maximum power ($V \approx 40$ V, $I \approx 9$ A, and $G \approx 900$ W/m^2), Eq. (8) yields a relative standard uncertainty of approximately 2.9%, corresponding to an expanded uncertainty of approximately 5.8% for $k = 2$. The main contribution comes from the irradiance, whose calibration standard uncertainty corresponds to about 2.1% of the measured value, followed by the contribution of the current, whose standard uncertainty of 0.1633 A represents about 1.8%.

For the thermal efficiency, the relative uncertainty depends on the circulation regime and, mainly, on the measured mass flow rate. According to Table 1, the standard uncertainty of the flow rate is 0.0001 L/s, equivalent to approximately 0.1 g/s for water. Under natural circulation, with $\dot{m} \approx 7$ g/s, this component corresponds to about 1.4% of the measured value. Under forced circulation, for $\dot{m} \approx 110$ g/s, the flow-rate contribution decreases to about 0.09%. Thus, although the flow rate remains the most relevant uncertainty source in the thermosiphon regime, its contribution, according to the values presented in Table 1, is significantly lower than previously estimated. The contributions of the temperature difference $(T_o - T_i)$ and of the irradiance must also be considered through Eq. (9), so that the final thermal-efficiency uncertainty depends on the temperature differential observed in each operating condition.

C. Acquisition Reliability in Continuous Operation

The tests conducted over 22 consecutive days of operation total 30,297 samples [12]. The median sampling period was 59 s, with a global completeness of 99.1% relative to the expected number of samples and only two gaps longer than 5 minutes (the largest at 15.8 min), attributed to power outages in the alternating-current (AC) distribution grid, which temporarily shut down the system. The spurious temperature samples (outside the physical range of 0 to 90 °C, e.g. readings of -127 °C typical of a transient failure of the 1-Wire bus) amounted to only 6 records, i.e. 0.02% of the total and concentrated on a single day, being removed by range filtering in post-processing, leaving 30,291 valid samples. Figure 5 presents the daily completeness of the acquisition.

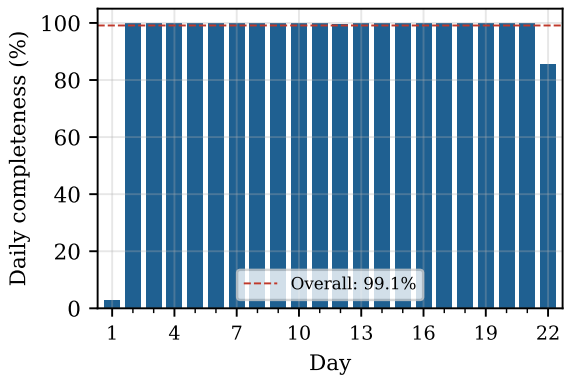

FIGURE 5. Daily completeness of the data acquisition over the 22-day campaign (day 1: 29 September 2024), relative to the expected number of samples (one per minute). The dashed line indicates the overall completeness (99.1%); the low values on the first and last days correspond to the start of the acquisition (at 23:22) and to its interruption for inspection of the system.

The graph shows that the first day exhibits low completeness (approximately zero) due to the start of data acquisition at 23:22. On the last day, the absence of records is associated with the interruption of the collection to analyze the operation of the acquisition system, totaling 20 complete days of data.

D. Electrical Model Validation with Real Data

The plant modules are the Canadian Solar HiKu CS3W-425P ($P_{STC} = 425$ W, $\gamma = -0.36\,\%/°\mathrm{C}$, NMOT $= 42$ °C,

effective area of 1.984 m^2 per module). Model (2)–(3) was compared with the measurements as 5-minute averages, under significant-irradiance conditions ($G > 50$ W/m^2). The factor k of each module was identified by least squares, and the resulting errors are listed in Table 2. Since k is a single scalar parameter fitted over several thousand samples, the model has a very low risk of overfitting and the reported metrics, although computed over the identification set, are representative of the model's predictive ability. This was confirmed by a 70/30 hold-out test repeated over 200 random partitions: identifying k on 70% of the samples changed its value by a median of 0.2% (at most 1.2%) relative to the fit with all data, and the mean R^2 evaluated on the remaining 30% (0.89–0.90 depending on the module; range 0.82–0.96) matched the training R^2, indicating no appreciable in-sample optimism. Figure 6(a) shows the dispersion between measured and modeled power for module PV2, and Figure 6(b) the comparison of the time series on a day with cloudiness transients, showing that the model follows the dynamics of the irradiance. The identified performance factors (k between 0.84 and 0.89) lump together losses from soiling, cabling, mismatch, and MPP deviation, being consistent with derating factors reported in the literature for operating plants [22]. In terms of energy, the model predicts the daily generation of each module with a mean absolute error between 4.7% and 7.6%, and the total energy of the period with an error below 3% (e.g. PV2: 34.4 kWh measured vs. 33.7 kWh modeled). These results demonstrate that the proposed DAQ provides data of sufficient quality for the calibration and validation of generation models, an application stated but not demonstrated in [11].

TABLE 2. Electrical model validation (5-min averages, $G > 50$ W/m^2).

Module	k	RMSE (W)	MAPE (%)	R^2	MAPE E_{day} (%)
PV1	0.869	31.5	13.3	0.89	7.0
PV2	0.886	31.5	14.0	0.89	7.6
PVT1	0.843	29.4	10.4	0.89	4.7
PVT2	0.873	29.2	8.9	0.90	4.7

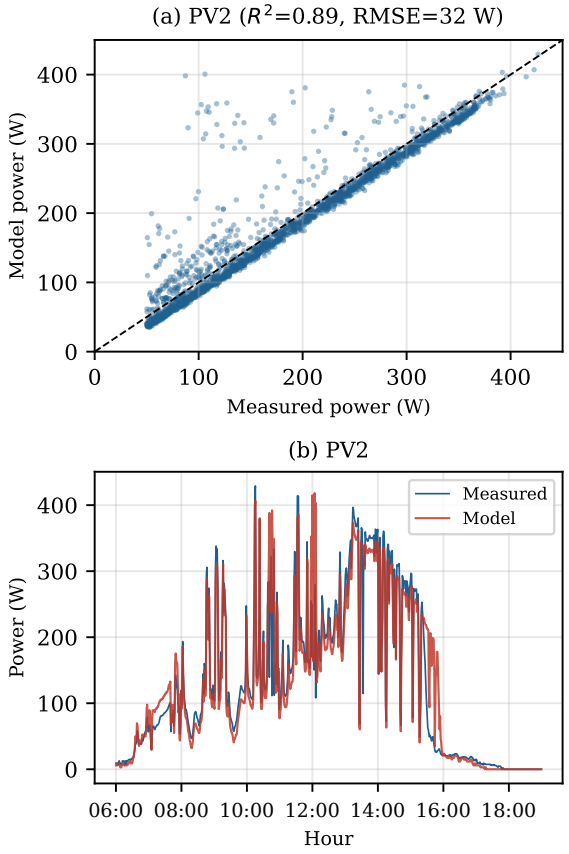

FIGURE 6. Validation of the temperature-corrected electrical model for module PV2: (a) scatter plot of the modeled versus the measured power (5-min averages), with the dashed line indicating the ideal 1:1 agreement; (b) measured and modeled power over a day with cloud transients.

E. Collector Thermal Characterization

The Hottel–Whillier curve (7) presumes a forced, constant, and known flow rate, a condition satisfied only in the forced-circulation test with a pump. In thermosiphon mode, the flow rate is low, variable, and self-induced by the temperature difference itself, so that the parameters $F_R(\tau\alpha)$ and F_RU_L would lose physical meaning. For this reason, as described in Subsection C, the collector model was fitted exclusively with the data from a single day, under forced circulation. Applying the least-squares fit of (7) to the 5-min windows in which the pump was running throughout, with $G > 400$ W/m^2 and discarding the first 15 min after the pump start-up, $F_R(\tau\alpha) = 0.289 \pm 0.008$ and $F_RU_L = 14.9 \pm 0.7$ W/(m^{2}K) were obtained (± 1 standard error, 64 windows), Figure 7. The coefficient of determination is $R^2 = 0.87$, and the parameters are stable with respect to the averaging window: windows of 10 and 15 min yield $F_R(\tau\alpha) = 0.292$ and F_RU_L between 15.1 and 15.2 W/(m^{2}K), with R^2 of 0.95 and 0.97, respectively. The residual dispersion is consistent with the transient nature of the test: with the pump running continuously and no hot-water consumption, the reservoir warmed progressively over the day, raising the inlet temperature T_i and moving the system away from the quasi-steady-state condition presumed by the equation. It is, moreover, a single test day. Rather than a limitation, obtaining these parameters from a single test day illustrates the system's capability to extract physical information from occasional campaigns; additional tests, which are trivially executable in the permanent installation, would refine the parameters and the non-steady dynamics. It should be noted that, as they stem from a single test in a transient regime, the values of $F_R(\tau\alpha)$ and F_RU_L should be interpreted as an in-situ estimate rather than a certification-grade characterization. Accordingly, the single-day basis means that these parameters are not a validated steady-state characterization of the collector and should not be extrapolated to operating

CC BY

conditions far from those of the test, in particular to other flow rates; in line with the purpose of this work, they are used to obtain first-order design estimates and to illustrate the capability of the acquisition system. A full identification requires dedicated multi-day forced-circulation campaigns at fixed flow rates and controlled inlet temperature, which the permanent installation makes straightforward and which are proposed as future work.

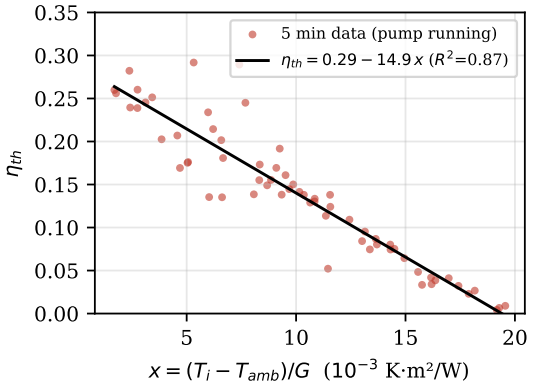

FIGURE 7. Hottel–Whillier curve of the PV/T collector, identified in the forced-circulation test with a pump (5-min averages with the pump running, $G > 400$ W/m^2).

F. Forced-Circulation Simulation over the Thermosiphon Days

With the collector model identified in the pump test (Subsection E), a design question is addressed: how much would forced circulation increase the captured thermal energy relative to thermosiphon? The forced model ($F_R(\tau\alpha) = 0.289$; $F_R U_L = 14.9$ W/m^{2}K) is fed with the real series of irradiance, ambient temperature, and inlet temperature measured on each of the 18 thermosiphon days, estimating the useful heat that forced circulation would have captured, $\hat{Q}_u = S_{th}\,[F_R(\tau\alpha)\,G - F_R U_L\,(T_i - T_{amb})]$, with the pump active for $G > 50$ W/m^2. This simulated energy is compared with the thermal energy *actually measured* in thermosiphon mode on the same days. It is, therefore, a simulation in which a single model (that of the collector under the pump) is confronted with the real measurement, without additional assumptions about the thermosiphon regime. Table 3 and Figure 8 summarize the result. Summed over the 18 days, the thermal energy would rise from 46.5 kWh (measured thermosiphon) to 91.0 kWh (simulated forced circulation), a gross gain of 44.6 kWh (+96%). Deducting the pumping consumption (45 W over 174 h, or 7.8 kWh), the net gain is 36.7 kWh (+79%). Figure 8(b) shows the cumulative energy over the period: the distance between the measured and simulated curves, highlighted by the shaded area, widens progressively and corresponds to the accumulated gross gain of forced circulation. On all 18 days the simulated forced circulation exceeds the measured thermosiphon. The two Sundays excluded from the comparison, on which the pump was operated by its timer at ≈43 g/s, provide an independent check of the collector model at a flow rate different from that of the identification test: on 6 October (daily irradiation of 5.0 kWh/m^2), the model predicted 3.92 kWh against 3.76 kWh measured (+4%); on 13 October, with very low irradiation (1.6 kWh/m^2), the prediction was 0.54 kWh against 0.96 kWh measured, a large relative error on a small absolute energy. It is emphasized that this estimate

TABLE 3. Thermal energy (18 thermosiphon days): measured vs. forced circulation simulated by the collector model.

Scenario	E_{th} (kWh)
Thermosiphon (measured)	46.5
Forced circulation (simulated, gross)	91.0
Pumping consumption (45 W, 174 h)	−7.8
Forced circulation (net)	83.2
Gross gain	+44.6 (+96%)
Net gain	+36.7 (+79%)

constitutes an upper bound, since the model applies the inlet temperature measured in thermosiphon mode; under real forced circulation, the greater capture would progressively raise the reservoir temperature and, therefore, T_i, reducing the gain potentially significantly. This feedback effect is precisely what is observed in the pump test and quantified in the control simulation that follows. The collector model makes this dependence explicit through its loss term $F_R U_L(T_i - T_{amb})$: each 1 °C increase in T_i reduces the simulated useful heat by $S_{th}\,F_R U_L \approx 54$ W. On the thermosiphon days, T_i was practically equal to the ambient temperature (mean difference below 0.1 °C), because the collector draws water from the bottom of the stratified boiler. Raising the mean T_i in the simulation by 1, 2, and 3 °C reduces the gross gain to +76%, +58%, and +40%, respectively, and the gain vanishes for an increase of about 5.8 °C. In the pump test, without hot-water consumption, T_i rose from 28.9 to 45.1 °C, remaining on average 9.3 °C above ambient, well beyond this value. The benefit of forced circulation therefore depends on hot-water consumption, which replenishes the system with cold water and keeps T_i low; without consumption, it may vanish altogether, which is consistent with the control simulation. The statistical uncertainties are smaller than this effect: propagating a ±1-standard-error variation of $F_R(\tau\alpha)$ and $F_R U_L$ yields gross gains between +90% and +102% (net between +74% and +85%), the averaging window changes the result by less than 2 percentage points, and a residual offset of ±0.1 °C between the temperature sensors changes it by at most about ±10 percentage points (Subsection B). The reported +96% gross / +79% net figures should therefore be read as the *potential* ceiling of the forced-circulation benefit under the measured low-T_i conditions, not as a guaranteed operational gain. Quantifying the realistic gain, with a closed collector–reservoir energy

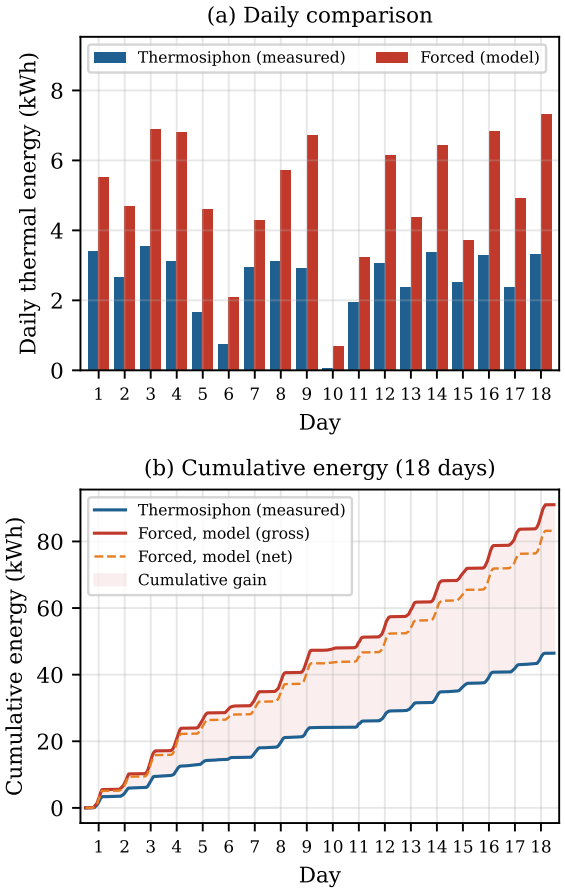

FIGURE 8. Forced-circulation simulation over the 18 thermosiphon days (numbered consecutively, excluding the two days with the pump on timer): (a) daily thermal energy measured (thermosiphon) vs. simulated by the collector model (forced); (b) cumulative thermal energy, with the net scenario deducting the pumping consumption. The shaded area in (b) highlights the cumulative gross gain, i.e. the area between the measured (thermosiphon) and simulated (forced) curves.

balance and a hot-water consumption profile, is identified as future work.

G. Pump-Actuation Control Simulation

As a further demonstration of the possibilities opened by the acquisition system, a pump-actuation control strategy is evaluated here. The forced-circulation test was conducted with the pump running continuously between 09:00 and 15:00, without hot-water consumption. Figure 9 reveals the consequence of this operation: the captured thermal power is high in the early morning, when the reservoir is cold, but decays over the day as the boiler warms up: around 14:00, with T_o close to T_i, the capture is practically null, although the pump keeps consuming energy. That is, kept on indiscriminately, the pump wastes pumping when the reservoir is already saturated.

This behavior motivates a simple control strategy: switch off the pump when the temperature difference $T_o - T_i$ becomes small, indicating that the capture has dropped well

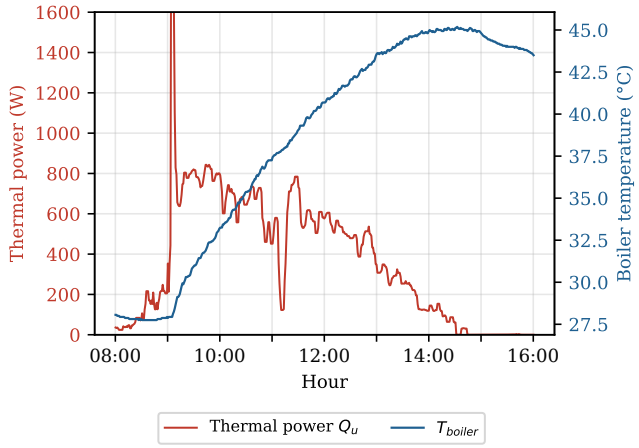

FIGURE 9. Dynamics of the forced-circulation test (Sept 27): captured thermal power and boiler temperature over the day. With the pump running continuously, the reservoir saturates and the capture decays in the afternoon.

below its earlier level, so that further pumping adds little energy at the cost of operating hours and wear. The threshold was set at $T_o - T_i \geq 0.5$ °C. This value is well above the 12-bit resolution of the sensors (0.0625 °C) and the residual inter-sensor offset considered in Subsection B (0.1 °C), so that switching is not triggered by measurement noise. A sensitivity analysis over the test data shows that thresholds of 0.25, 0.5, 0.75, and 1.0 °C preserve, respectively, 100%, 98%, 91%, and 84% of the net thermal energy, while reducing the pumping hours by 15%, 24%, 36%, and 44%. The value of 0.5 °C lies at the knee of this trade-off: it is the largest threshold that preserves practically all the net energy (loss of at most 2%) while substantially reducing the pumping hours. It is worth stressing that this is a post-processing simulation applied to the measured data of the forced-circulation test, used to quantify the potential benefit of the strategy; it was not deployed as a real-time controller on the plant. Its embedded implementation and experimental validation are proposed as future work. Applying this threshold over the measured test data, two strategies are compared, pump running continuously (as in the real test) and controlled pump, directly from the thermal energy actually measured, without resorting to models of the thermosiphon regime. Table 4 and Figure 10 present the results.

TABLE 4. Simulation for two pump-actuation strategies.

Strategy	E_{th} (kWh)	E_{pump} (kWh)	E_{net} (kWh)	Hours
Continuous pump	2.93	0.27	2.66	5.9
Control ($\Delta T \geq 0.5$ °C)	2.81	0.20	2.61	4.5

The ΔT control preserves 98% of the net thermal energy captured (2.61 vs. 2.66 kWh) while reducing the pumping hours by 24% (4.5 vs. 5.9 h), which lowers the electrical consumption and the mechanical wear of the pump. The

CC BY

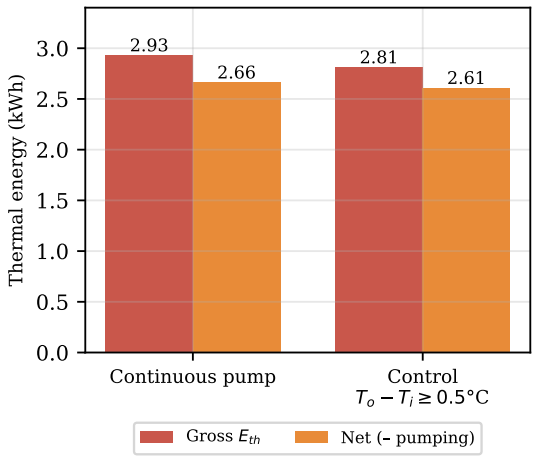

FIGURE 10. Control simulation: gross and net thermal energy of the pump-actuation strategies.

energy gain is modest because, in the test, the capture is intrinsically limited by the reservoir saturation. It should be noted that this limit stems from the absence of hot-water consumption during the test: in real residential use, consumption throughout the day replenishes cold water into the system, lowering T_i, restoring the $T_o - T_i$ gradient, and thus increasing both the capture and the benefit of the control.

V. CONCLUSIONS

This work presented a data acquisition system for PV and PV/T plants, quantitatively demonstrating its suitability for scientific and engineering applications. Over 22 days of continuous operation, the system achieved 99.1% completeness with only 0.02% of spurious samples. As demonstrations of the system's capabilities, the collected data made it possible to: validate a temperature-corrected electrical model, with a daily energy error between 4.7% and 7.6% per module and effective performance factors between 0.84 and 0.89; experimentally characterize the PV/T collector from a forced-circulation test ($F_R(\tau\alpha) = 0.289$; $F_R U_L = 14.9$ W/m^{2}K); and quantify the efficiency uncertainties, which remain below 6% ($u(\eta_{el}) \approx 2.9\%$; $u(\eta_{th}) \approx 2.7\%$ in thermosiphon mode), demonstrating that the system provides figures of merit with reliability adequate for engineering studies.

From the collector model fed with the real series, forced circulation was simulated over the 18 thermosiphon days, estimating a potential thermal energy gain of about 96% (79% net of pumping consumption), an upper bound that does not account for the rise of the inlet temperature under forced circulation; this gain depends on hot-water consumption and vanishes if forced circulation raises the mean inlet temperature by about 6 °C. A control simulation showed, however, that this gain is conditional on the actuation strategy: the pump kept continuously on saturates the reservoir and wastes pumping, whereas an actuation controlled by the temperature difference $T_o - T_i$ preserves the captured energy with lower consumption and less wear. More than the pointwise values (which inherit the uncertainty of a single, transient test), the set of models validated with real data and the reliable acquisition flow establish the elements needed for embedded, model-based monitoring and control of the system.

It is worth highlighting that all these developments are enabled by the acquisition infrastructure presented here: as it is permanently installed and operating, it turns occasional studies into continuous investigation capability. As future work, the following are proposed: the embedded implementation of the validated models on the ESP32, incorporating a realistic consumption profile and a complete collector/reservoir thermal coupling, for optimal pump actuation and anomaly detection, including the experimental validation of the pump-control strategy; a paired calibration of the inlet and outlet temperature sensors, to bound the residual error of the differential measurement; dedicated campaigns with multiple days of forced circulation under controlled consumption, at fixed flow rates and controlled inlet temperature, which would refine the collector parameters; a side-by-side campaign with two additional PV/T systems, currently being acquired, operating simultaneously with and without forced circulation under the same irradiance and ambient temperature, to experimentally validate the simulated gain; the modeling of the system dynamics through neural networks trained with the temporal dataset; and the use of the open dataset [12] for the prediction of electrical and thermal generation.

ACKNOWLEDGMENT

We acknowledge the Espírito Santo Research and Innovation Support Foundation (FAPES) and the National Council for Scientific and Technological Development (CNPq) for their financial support in the projects: FAPES 2022-BWBR2, FAPES 2024-GP4XW, FAPES 2024-1FNPM, CNPq 301349/2025-8, and CNPq 311894/2025-9.

AUTHOR'S CONTRIBUTIONS

C.R.COUTINHO: Conceptualization, Data Curation, Formal Analysis, Investigation, Methodology, Validation, Writing – Original Draft, Writing – Review & Editing. **R.FIOROTTI:** Formal Analysis, Writing – Review & Editing. **G.B.COUTINHO:** Data Curation, Investigation, Validation. **J.F.FARDIN:** Supervision, Writing – Review & Editing. **H.R.O.ROCHA:** Supervision, Writing – Review & Editing.

PLAGIARISM POLICY

This article was submitted to the similarity system provided by Crossref and powered by iThenticate – Similarity Check.

DATA AVAILABILITY

The data used in this research is available in the body of the document.

REFERENCES

[1] Empresa de Pesquisa Energética (EPE), *Balanço Energético Nacional 2024: Relatório Síntese*, Empresa de Pesquisa Energética, Rio de Janeiro, Brasil, mar 2024, URL: https://www.epe.gov.br/sites-pt/publicacoes-dados-abertos/publicacoes/PublicacoesArquivos/publicacao-819/topico-723/BEN2024.pdf, accessed on: Jan. 12, 2025.

[2] P. Dwivedi, K. Sudhakar, A. Soni, E. Solomin, I. Kirpichnikova, "Advanced cooling techniques of PV modules: A state of art", *Case Studies in Thermal Engineering*, vol. 21, p. 100674, Oct. 2020, doi:10.1016/j.csite.2020.100674.

[3] S. S. Joshi, A. S. Dhoble, "Photovoltaic-Thermal systems (PVT): Technology review and future trends", *Renewable and Sustainable Energy Reviews*, vol. 92, pp. 848–882, Sep. 2018, doi:10.1016/j.rser.2018.04.067.

[4] M. Samykano, "Hybrid photovoltaic thermal systems: Present and future feasibilities for industrial and building applications", *Buildings*, vol. 13, no. 8, p. 1950, Aug. 2023, doi:10.3390/buildings13081950.

[5] A. L. Abdullah, S. Misha, N. Tamaldin, M. A. M. Rosli, F. A. Sachit, "Theoretical study and indoor experimental validation of performance of the new photovoltaic thermal solar collector (PVT) based water system", *Case Studies in Thermal Engineering*, vol. 18, p. 100595, Apr. 2020, doi:10.1016/j.csite.2020.100595.

[6] V. F. Do Nascimento, I. Yahyaoui, R. Fiorotti, A. E. A. Amorim, I. C. Belisário, C. E. S. Abreu, H. R. O. Rocha, F. Tadeo, "Dimensioning and efficiency evaluation of a hybrid photovoltaic thermal system in a tropical climate region", *Sustainable Energy, Grids and Networks*, vol. 32, p. 100954, Dec. 2022, doi:10.1016/j.segan.2022.100954.

[7] M. T. Ahmed, M. R. Rashel, M. Islam, A. K. M. K. Islam, M. Tlemcani, "Classification and parametric analysis of solar hybrid PVT system: A review", *Energies*, vol. 17, no. 3, p. 588, Feb. 2024, doi:10.3390/en17030588.

[8] M. Fuentes, M. Vivar, J. M. Burgos, J. Aguilera, J. A. Vacas, "Design of an accurate, low-cost autonomous data logger for PV system monitoring using Arduino™ that complies with IEC standards", *Solar Energy Materials and Solar Cells*, vol. 130, pp. 529–543, Nov. 2014, doi:10.1016/j.solmat.2014.08.008.

[9] A. López-Vargas, M. Fuentes, M. V. García, F. J. Muñoz-Rodríguez, "Low-cost datalogger intended for remote monitoring of solar photovoltaic standalone systems based on Arduino™", *IEEE Sensors Journal*, vol. 19, no. 11, pp. 4308–4320, Jun. 2019, doi:10.1109/JSEN.2019.2898667.

[10] A. López-Vargas, M. Fuentes, M. Vivar, "IoT application for real-time monitoring of solar home systems based on Arduino™ with 3G connectivity", *IEEE Sensors Journal*, vol. 19, no. 2, pp. 679–691, Jan. 2019, doi:10.1109/JSEN.2018.2876635.

[11] C. R. Coutinho, R. Fiorotti, H. R. de Oliveira Rocha, J. F. Fardin, A. L. d. S. Merlin, "Data Acquisition System in a Photovoltaic and Photovoltaic/Thermal Plant", *in 2025 Brazilian Power Electronics Conference (COBEP)*, pp. 1–5, Vitória, Brazil, Oct. 2025, doi:10.1109/COBEP66423.2025.11231690.

[12] C. R. Coutinho, R. Fiorotti, H. Rocha, J. F. Fardin, "Data PVT", Mendeley Data, V3, January 2026, doi:10.17632/xwcyp5j9pz.3.

[13] K. Nguyen-Vinh, S. Gonapaladeniya, N. Nguyen-Quang, Z. Leonowicz, "A Review of Photovoltaic Technology", *in 2024 24th International Scientific Conference on Electric Power Engineering (EPE)*, pp. 1–6, IEEE, May 2024, doi:10.1109/EPE61521.2024.10559575.

[14] R. Fiorotti, J. F. Fardin, H. R. O. Rocha, D. Rua, J. A. P. Lopes, "Day-ahead optimal scheduling considering thermal and electrical energy management in smart homes with photovoltaic–thermal systems", *Applied Energy*, vol. 374, p. 124070, Nov. 2024, doi:10.1016/j.apenergy.2024.124070.

[15] D. L. Evans, "Simplified method for predicting photovoltaic array output", *Solar Energy*, vol. 27, no. 6, pp. 555–560, Dec. 1981, doi:10.1016/0038-092X(81)90051-7.

[16] L. d. O. Santos, P. C. M. de Carvalho, C. de Oliveira Filho, "Photovoltaic Cell Operating Temperature Models: A Review of Correlations and Parameters", *IEEE Journal of Photovoltaics*, vol. 12, no. 1, pp. 179–190, Jan. 2022, doi:10.1109/JPHOTOV.2021.3113156.

[17] S. A. Kalogirou, *Solar Energy Engineering: Processes and Systems*, 3 ed., Academic Press (Elsevier), Cambridge, MA, USA, Dec. 2023, ISBN: 978-0-323-99350-0.

[18] F. Maoulida, R. Djedjig, M. A. Kassim, M. El Ganaoui, "Numerical study for the evaluation of the effectiveness and benefits of using photovoltaic-thermal (PV/T) system for hot water and electricity production under a tropical African climate: Case of Comoros", *Energies*, vol. 16, no. 1, p. 240, Jan. 2023, doi:10.3390/en16010240.

[19] P. K. Pathak, D. G. Roy, A. K. Yadav, S. Padmanaban, F. Blaabjerg, B. Khan, "A state-of-the-art review on heat extraction methodologies of photovoltaic/thermal system", *IEEE Access*, vol. 11, pp. 49738–49759, May 2023, doi:10.1109/ACCESS.2023.3277728.

[20] JCGM, *Evaluation of measurement data — Guide to the expression of uncertainty in measurement (GUM)*, Joint Committee for Guides in Metrology, Sep. 2008, doi:10.59161/JCGM100-2008E, jCGM 100:2008.

[21] International Organization for Standardization, *ISO 9806:2017 — Solar energy — Solar thermal collectors — Test methods*, ISO, Geneva, Switzerland, Sep. 2017.

[22] B. Marion, J. Adelstein, K. Boyle, H. Hayden, B. Hammond, T. Fletcher, B. Canada, D. Narang, D. Shugar, H. Wenger, A. Kimber, L. Mitchell, G. Rich, T. Townsend, "Performance Parameters for Grid-Connected PV Systems", *in Conference Record of the 31st IEEE Photovoltaic Specialists Conference*, pp. 1601–1606, Lake Buena Vista, FL, USA, Jan. 2005, doi:10.1109/PVSC.2005.1488451.

Carlos R. Coutinho received the B.S. degree in electrical engineering with a specialization in telecommunications from Faculdade Novo Milênio, Vila Velha, Brazil, in 2009, and the specialization degree in informatics in education from the Instituto Federal do Espírito Santo (Ifes), Brazil, in 2013. He is currently a Professor with Ifes, Campus São Mateus, São Mateus, Brazil, where he coordinates the electrical engineering undergraduate program and teaches in the electrical engineering and in the integrated and concomitant technical programs in electrotechnics.

Rodrigo Fiorotti received the B.S. and M.S. degrees in electrical engineering from the Federal University of Espírito Santo (UFES), Vitória, Brazil, in 2013 and 2015, respectively. He is currently a full-time Professor with the Instituto Federal do Espírito Santo (Ifes) and a doctoral candidate with the Graduate Program in Electrical Engineering (PPGEE), UFES. His main research interests include electrical power systems, alternative energy sources, smart grids, demand-side management, and energy efficiency.

Gustavo B. Coutinho is currently pursuing the B.S. degree in electrical engineering with the Instituto Federal do Espírito Santo (Ifes), Campus São Mateus, São Mateus, Brazil.

Jussara F. Fardin received the B.S. degree in electrical engineering from the Federal University of Espírito Santo (UFES), Vitória, Brazil, in 1978, the M.S. degree in electrical engineering from the Pontifical Catholic University of Rio de Janeiro, Brazil, in 1983, and the Ph.D. degree in electrical engineering from the University of Campinas, Brazil, in 2001. She is currently a Full Professor with UFES. Her research interests include renewable energy sources, microgrids, smart grids, system identification, and superconductivity applied to energy systems.

Helder R. de O. Rocha received the B.S. degree in electrical engineering and the M.S. and D.Sc. degrees in computer science from the Fluminense Federal University (UFF), Niterói, Brazil. He is currently with the Department of Electrical Engineering, Federal University of Espírito Santo (UFES), Vitória, Brazil. His research interests include optimization and artificial intelligence applied to smart grids and telecommunication systems. He is a fellow of the National Council for Scientific and Technological Development (CNPq).